REPORT DOCUMENTATION PAGE

Form Approved OMB NO. 0704-0188

The public reporting burden for this collection of information is estimated to average 1 hour per response, including the time for reviewing instructions, searching existing data sources, gathering and maintaining the data needed, and completing and reviewing the collection of information. Send comments regarding this burden estimate or any other aspect of this collection of information, including suggesstions for reducing this burden, to Washington Headquarters Services, Directorate for Information Operations and Reports, 1215 Jefferson Davis Highway, Suite 1204, Arlington VA, 22202-4302. Respondents should be aware that notwithstanding any other provision of law, no person shall be subject to any oenalty for failing to comply with a collection of information if it does not display a currently valid OMB control number.
PLEASE DO NOT RETURN YOUR FORM TO THE ABOVE ADDRESS.

1. REPORT DATE (DD-MM-YYYY)	2. REPORT TYPE	3. DATES COVERED (From - To)
	New Reprint	-

4. TITLE AND SUBTITLE
Friction Stir Weld Failure Mechanisms in Aluminum-Armor Structures Under Ballistic Impact Loading Conditions

5a. CONTRACT NUMBER
W911NF-11-1-0207

5b. GRANT NUMBER

5c. PROGRAM ELEMENT NUMBER
622105

6. AUTHORS
M. Grujicic, B. Pandurangan, A. Arakere, C-F. Yen, B. A. Cheeseman

5d. PROJECT NUMBER

5e. TASK NUMBER

5f. WORK UNIT NUMBER

7. PERFORMING ORGANIZATION NAMES AND ADDRESSES
Clemson University
Office of Sponsored Programs
300 Brackett Hall, Box 345702
Clemson, SC 29634 -5702

8. PERFORMING ORGANIZATION REPORT NUMBER

9. SPONSORING/MONITORING AGENCY NAME(S) AND ADDRESS(ES)
U.S. Army Research Office
P.O. Box 12211
Research Triangle Park, NC 27709-2211

10. SPONSOR/MONITOR'S ACRONYM(S)
ARO

11. SPONSOR/MONITOR'S REPORT NUMBER(S)
57228-EG.11

12. DISTRIBUTION AVAILIBILITY STATEMENT
Approved for public release; distribution is unlimited.

13. SUPPLEMENTARY NOTES
The views, opinions and/or findings contained in this report are those of the author(s) and should not contrued as an official Department of the Army position, policy or decision, unless so designated by other documentation.

14. ABSTRACT
A critical assessment is carried out of the microstructural changes in respect of the associated reductions in material mechanical properties and of the attendant ballistic-impact failure mechanisms in prototypical friction stir welding (FSW) joints found in armor structures made of high-performance aluminum alloys (including solution-strengthened and age-hardenable aluminum alloy grades). It is argued that due to the large width of FSW joints found in thick aluminum-armor weldments, the overall ballistic performance of

15. SUBJECT TERMS
aluminum armor, ballistic limit, failure mechanisms,friction stir welding

16. SECURITY CLASSIFICATION OF:			17. LIMITATION OF ABSTRACT	15. NUMBER OF PAGES	19a. NAME OF RESPONSIBLE PERSON
a. REPORT	b. ABSTRACT	c. THIS PAGE			Mica Grujicic
UU	UU	UU	UU		19b. TELEPHONE NUMBER: 864-656-5639

Report Title

Friction Stir Weld Failure Mechanisms in Aluminum-Armor Structures Under Ballistic Impact Loading Conditions

ABSTRACT

A critical assessment is carried out of the microstructural changes in respect of the associated reductions in material mechanical properties and of the attendant ballistic-impact failure mechanisms in prototypical friction stir welding (FSW) joints found in armor structures made of high-performance aluminum alloys (including solution-strengthened and age-hardenable aluminum alloy grades). It is argued that due to the large width of FSW joints found in thick aluminum-armor weldments, the overall ballistic performance of the armor is controlled by the ballistic limits of its weld zones (e.g., heat-affected zone, the thermomechanically affected zone, the nugget, etc.). Thus, in order to assess the overall ballistic survivability of an armor weldment, one must predict/identify welding-induced changes in the material microstructure and properties, and the operative failure mechanisms in different regions of the weld. Toward this end, a procedure is proposed in the present study which combines the results of the FSW process modeling, basic physical-metallurgy principles concerning microstructure/property relations, and the fracture mechanics concepts related to the key blast/ballistic-impact failure modes. The utility of this procedure is demonstrated using the case of a solid-solution strengthened and cold-worked aluminum alloy armor FSW-weld test structure.

REPORT DOCUMENTATION PAGE (SF298)
(Continuation Sheet)

Continuation for Block 13

ARO Report Number 57228.11-EG
Friction Stir Weld Failure Mechanisms in Alumin ...

Block 13: Supplementary Note
© 2013 . Published in Journal of Materials Engineering and Performance, Vol. Ed. 0 22, (1) (2013), (, (1). DoD Components reserve a royalty-free, nonexclusive and irrevocable right to reproduce, publish, or otherwise use the work for Federal purposes, and to authroize others to do so (DODGARS §32.36). The views, opinions and/or findings contained in this report are those of the author(s) and should not be construed as an official Department of the Army position, policy or decision, unless so designated by other documentation.

Approved for public release; distribution is unlimited.

JMEPEG (2013) 22:30–40
DOI: 10.1007/s11665-012-0239-7
©ASM International
1059-9495/$19.00

Friction Stir Weld Failure Mechanisms in Aluminum-Armor Structures Under Ballistic Impact Loading Conditions

M. Grujicic, B. Pandurangan, A. Arakere, C-F. Yen, and B.A. Cheeseman

(Submitted January 12, 2012; in revised form April 3, 2012; published online May 1, 2012)

A critical assessment is carried out of the microstructural changes in respect of the associated reductions in material mechanical properties and of the attendant ballistic-impact failure mechanisms in prototypical friction stir welding (FSW) joints found in armor structures made of high-performance aluminum alloys (including solution-strengthened and age-hardenable aluminum alloy grades). It is argued that due to the large width of FSW joints found in thick aluminum-armor weldments, the overall ballistic performance of the armor is controlled by the ballistic limits of its weld zones (e.g., heat-affected zone, the thermomechanically affected zone, the nugget, etc.). Thus, in order to assess the overall ballistic survivability of an armor weldment, one must predict/identify welding-induced changes in the material microstructure and properties, and the operative failure mechanisms in different regions of the weld. Toward this end, a procedure is proposed in the present study which combines the results of the FSW process modeling, basic physical-metallurgy principles concerning microstructure/property relations, and the fracture mechanics concepts related to the key blast/ballistic-impact failure modes. The utility of this procedure is demonstrated using the case of a solid-solution strengthened and cold-worked aluminum alloy armor FSW-weld test structure.

Keywords aluminum armor, ballistic limit, failure mechanisms, friction stir welding

1. Introduction

In the context of military tactical and battlefield vehicles, aluminum alloys have been traditionally used both as monolithic light-weight armor and in the construction of the vehicle frame structures to which the armor is attached (Ref 1). For the most part, aluminum alloys used nowadays in military-vehicle applications do not suffer from solidification and/or liquation cracking (cracking caused by the melting of low melting-point phase(s) typically located along the alloy grain boundaries). Consequently, defect-free welded joints can be produced in armor/structural-grade aluminum alloys using conventional fusion welding processes. Nevertheless, ever-increasing requirements concerning vehicle blast-survivability and reliability/durability demand detailed understanding of the microstructure/property/performance relations and the extent of welding-induced reduction in mechanical properties within different regions of the welded joints. In addition, there is a continuing push towards the development of new armor/structural-grade aluminum alloys with enhanced ballistic limit (e.g., AA2139, a precipitation hardened quaternary Al-Cu-Mg-Ag alloy) and utilization of novel joining technologies. Friction stir welding (FSW), the subject of the present study, is one of the new (solid-state) welding processes being increasingly used in military-vehicle applications (Ref 2). Within FSW, a non-consumable hard-material welding tool is used to generate, within the workpiece material surrounding the tool/workpiece interface (via frictional-sliding and plastic-work dissipation) the heat necessary for successful welding (without causing local melting). It should be noted that the term ballistic limit used in the present study refers to the so-called V_{50} velocity, i.e., the projectile incident velocity at which the probability for target penetration is 50% (Ref 3).

A typical FSW set-up used in the fabrication of butt-joints is shown schematically in Fig. 1. Due to the fact that FSW is a fairly complex thermomechanical process which involves interactions between various deformation, energy-dissipation, and microstructure evolution phenomena, the material microstructure, and , hence, mechanical properties in the weld region are spatially diverse (Ref 4-11). Examination of the spatial distribution of material microstructure within the FSW joints typically reveals the presence of the following three weld zones (excluding the base metal, i.e., the portion of the weldment within which the material microstructure/properties are not altered by the joining process), Fig. 2: (a) the heat-affected zone (HAZ) which is located next to the base metal and in which changes in material microstructure/properties are solely caused by the thermal effects associated with FSW; (b) the thermomechanically affected zone (TMAZ) which is located closer than the HAZ to the workpiece components contact interface, and in which both the thermal and the mechanical aspects of the FSW process cause changes in the material

M. Grujicic, B. Pandurangan, and **A. Arakere**, Department of Mechanical Engineering, Clemson University, 241 Engineering Innovation Building, Clemson, SC 29634-0921; and **C-F. Yen** and **B.A. Cheeseman**, Army Research Laboratory—Survivability Materials Branch, Aberdeen, Proving Ground, MD 21005-5069. Contact e-mail: gmica@clemson.edu.

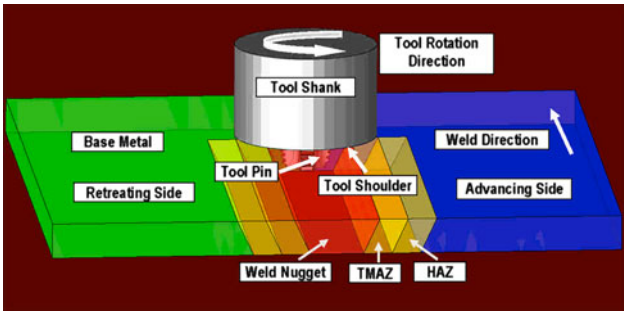

Fig. 1 A schematic of the FSW process

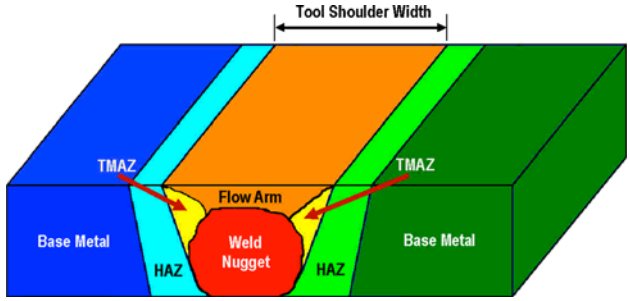

Fig. 2 A schematic of the main microstructural zones associated with the typical FSW joint

microstructure/properties; and (c) the weld *nugget* is the innermost zone of an FSW joint in which the material has been subjected to most severe conditions of plastic deformation and high-temperature exposure and consequently contains a very fine equiaxed grain dynamically recrystallized weld microstructure. In addition to the three FSW joint zones described above, in many alloy systems one observes the so-called "*flow arm*" zone. It is generally agreed that the fine grained material located in this zone is the one that was (during welding) temporarily residing underneath the FSW-tool shoulder with an upright truncated-conical profile.

Relative to the conventional fusion-welding processes, several advantages are offered by FSW. A fairly detailed account of these advantages was reported in our recent study (Ref 12) and, hence, will not be discussed here. However, specific advantages offered by FSW in the context of military vehicle armor structures will be discussed later in this section. As far as the general advantages of FSW are concerned, it should be noted that these advantages are due to the fact that FSW is a solid-state joining process and does not require the use of a filler metal, flux, or fuel/oxidizer. Therefore, FSW joints are associated with smaller changes in the material microstructure and smaller material property degradations. Owing to the advantages offered by FSW, this relatively new joining technology has already found large-scale applications in several industries. A detailed account of these applications has also been reported in our recent study (Ref 12).

Recent advances in the FSW technology and in high-performance aluminum alloys offer the potential for a dramatic improvement in ballistic performance, structural reliability, and durability of military vehicle armor structures. Among these recent developments, the following appear to be most noteworthy (Ref 13-20): (a) The ability to join aluminum alloy grades which were previously considered as "*non-weldable*"; (b) New high-power FSW machines are capable of joining aluminum-grade plates with thicknesses exceeding 100 mm (typically, aluminum armor plate thicknesses are in a 30 to 80 mm range); (c) Process control has enabled the production of high quality FSW joints with the strength and ductility levels comparable to those observed in multi-bead fusion welds; and (d) Development of new high-strength/high-toughness aluminum-alloy grade with significantly increased ballistic limit.

While the use of FSW helps one avoid the problems associated with solidification and liquation cracking, the standard problems related to the changes in material microstructure and reduction in mechanical properties (within the joints) observed in conventional fusion welding, also accompany FSW. In fact, these problems could be even more pronounced in the case of FSW of thick armor plates, which is typically carried out under low welding rates (to prevent tool breaking) and consequently, may produce unusually wide (e.g., 2-3 times the weldment thickness) HAZ. Thus, when designing FSW armor structures, one must account for a higher probability of direct ballistic impact on the weld. This problem may be even more serious considering the fact that in fusion welded armored structures the welds are typically of a fillet type and could be strategically placed to prevent them from being subjected to direct ballistic impact. On the other hand, geometric and kinematic constraints associated with FSW process often affect the final placement of the welds. These findings suggest that the changes in the material microstructure and the associated reduction in the mechanical properties within the welded joints may play a more prominent role in the overall ballistic performance (and structural durability) of the military-vehicle FSWed armor structures.

The main objective of the present study is to carry out a critical, semi-quantitative assessment of the microstructural changes, of the reductions in the mechanical properties and of the losses in the ballistic limit in different FSW joint zones encountered in the context of thick armor structures made of a prototypical high-performance age-hardenable aluminum alloy. Specifically, an attempt is made to establish relationships between the weld local microstructure, failure mode, and the resulting ballistic limit.

The organization of the article is as follows: A brief overview of the key failure mechanisms observed within FSW welds as a result of blast/ballistic impact is provided in Sect. 2. The mathematical models are presented and critically assessed in Sect. 3. In Sect. 4, A new procedure which combines the results of the FSW process modeling, basic physical-metallurgy principles concerning microstructure/property relations, and the fracture mechanics concepts related to the key blast/ballistic-impact failure modes is introduced and applied to a prototypical solution-strengthened aluminum alloy FSW joint to predict spatial distribution of the ballistic limit throughout the weld. The main conclusions resulting from the present study are summarized in Sect. 5.

2. FSW Joint Failure Mechanisms

Detailed experimental investigations of the mechanical response of FSW joints subjected to ballistic impact and reported in the open literature revealed the operation of the following main failure modes within the FSW joints (Ref 21-24): (a) front/impacted and back/rear face petaling; (b) ductile hole

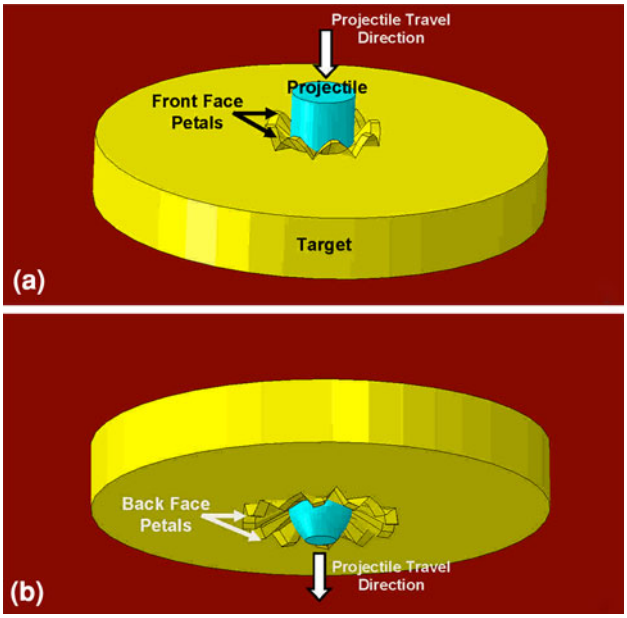

Fig. 3 Schematic representation of: (a) front face; and (b) back face petaling failure mechanism

enlargement; (c) plugging; and (d) spalling. In a specific ballistic-impact scenario, the dominant failure mode has been found to be controlled by factors such as (a) the impacted (HAZ, TMAZ, or weld nugget) weld-zone; (b) the local microstructure (e.g., grain-size, precipitate crystal structure, particle size, volume fraction, etc.) and mechanical properties (primarily hardness); and (c) projectile's mass, shape, size (relative to the target thickness), and hardness (relative to that of the target material). In the remainder of this section, brief descriptions are provided of the key features of the aforementioned four failure mechanisms.

2.1 Front/Impacted and Back/Rear Face Petaling

This type of failure mechanism is associated with partitioning of the target material surrounding the projectile into leaf/petal-like backward/forward projections formed at material heterogeneities/flaws. Schematics of the front face and the back face petaling failure mechanism are depicted in Fig. 3(a) and (b), respectively. Front face petaling is produced by high radial and circumferential tensile stresses within the target material surrounding the projectile which, in turn, are the result of the impact-induced (backward) bending moments within the target. In the case of rear face petaling, as the rear face of the target plate is pushed outward, a star-shaped crack is nucleated in front of the projectile head. The extension of this crack to the target back face produces discrete petal-like segments (Ref 25).

Failure of ballistic armor solely by petaling is not generally observed but rather petaling is found to accompany another mode of failure (typically the ductile hole enlargement or plugging failure mechanisms within the HAZ/TMAZ zones). It is often observed that while front-face petaling occurs under most ballistic-impact loading conditions, the extent of back-face petaling is affected by the target-material hardness. Specifically, as the HAZ/TMAZ material hardness increases and, thus, ductility decreases, back face petaling becomes less pronounced and progressively replaced by spalling. It is generally believed that in thick armor plates, petaling plays a

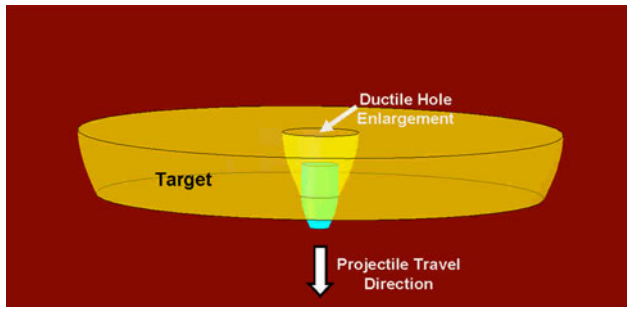

Fig. 4 Schematic representation of the ductile hole enlargement failure mechanism

minor role in defeating (i.e., in absorbing the kinetic energy carried by) the projectile. Consequently, petaling failure mechanism will not be discussed in great detail in the present study.

2.2 Ductile Hole Enlargement

This type of failure mechanism occurs when the projectile head (typically ogive shaped) causes radial displacement of the target material, and the resulting radial momentum transfer gives rise to a continuous enlargement of the resulting hole with the forward progress of the projectile (Ref 25). While the onset of this failure mechanism is affected by the projectile shape, size, velocity, and the target thickness, it is generally observed in the case of thicker targets impacted by ogive-shaped projectiles. A schematic of this mechanism is shown in Fig. 4. This mechanism is most often observed in the case of HAZ/TMAZ weld zones being impacted with sharp-tip, hard projectiles (e.g., 7.62 mm caliber, 8.2 g, ogival-nose, steel jacketed, hard tungsten core (1400 Hv), armor piercing (AP) projectile (Ref 1). As mentioned above, this failure mechanism is often accompanied by additional failure mechanisms taking place at the target front face and/or back face. The character and the extent of these additional failure modes is greatly affected by the target-material hardness. Specifically, in the case of (highly over-aged) low-hardness HAZ/TMAZ zones (near the weld center-line), ductile hole enlargement is normally accompanied only by front-face petaling. As the weld-zone hardness increases (i.e., as one moves away from the weld center-line), however, back face petaling first appears as an additional failure mode, only to be replaced with back face spalling at the highest HAZ/TMAZ hardness levels. The pronounced occurrence of back face spalling at the highest hardness levels is typically associated with a reduction in the through-the-thickness material fracture toughness (Ref 1).

A prototypical functional relationship between the target ballistic limit and the material local hardness in the case of the ductile hole enlargement-dominated failure, is depicted in Fig. 5(a). It is seen that, initially the ballistic limit increases (linearly) with an increase in target hardness. However, at high levels of the target hardness at which back face spallation begins to take place, a decrease in the ballistic limit with an increase in the material hardness is observed.

It should be noted that the material associated with the lowest level of hardness in Fig. 5(a) is in the severely over-aged condition (and found in the HAZ/TMAZ regions near the weld center-line). Typically, a loss of ballistic limit (relative to that found in the base metal) by less than 20% (if quantified using

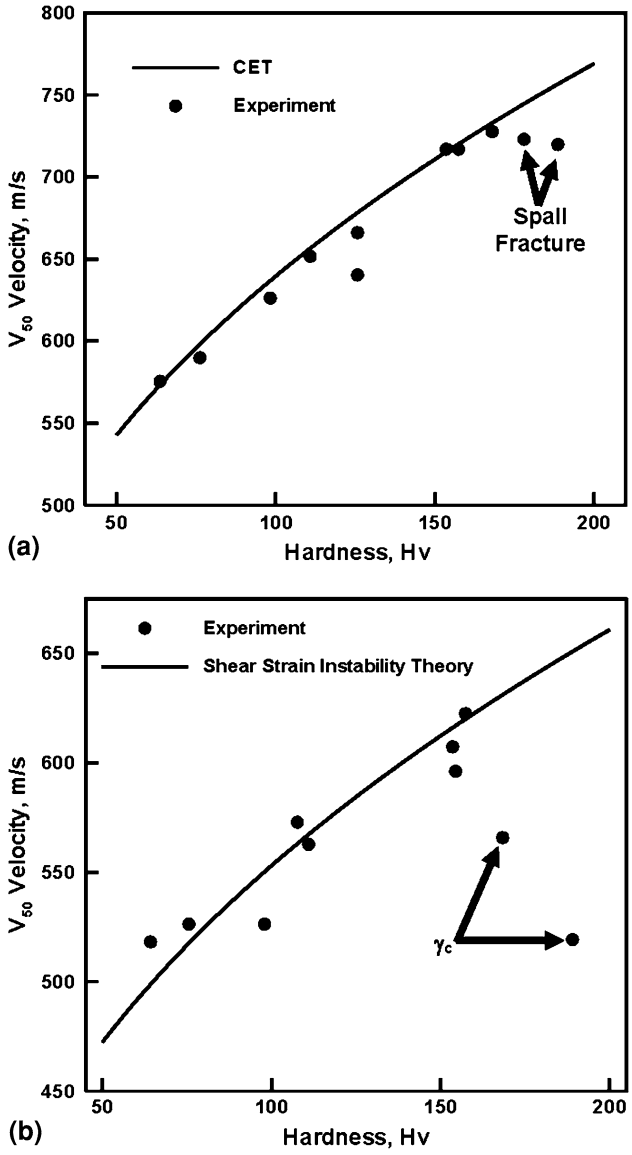

Fig. 5 A prototypical functional relationship between the target ballistic limit and the material local hardness: (a) in the case of the ductile hole enlargement-dominated failure obtained experimentally (Ref 1) and predicted by the CET; and (b) in the case of plugging-dominated failure obtained experimentally (Ref 1) and predicted by the plastic strain localization theory

V_{50}) or by less than 40% (if quantified using the projectile kinetic energy loss) is observed in this case.

2.3 Plugging

This type of failure mechanism is associated with the formation and ejection of a cylindrical slug with a diameter comparable with that of the projectile and is a result of intense localized shearing of the target material at the periphery of advancing projectile. A schematic of this mechanism is depicted in Fig. 6. This mechanism is the most often observed in the case of HAZ/TMAZ weld zones being impacted with blunt, lower hardness projectiles [e.g., 20-mm caliber, 53 g, blunt, chamfered right circular cylindrical steel fragment simulating projectile (FSP)]. As in the case of ductile hole enlargement, plugging is typically accompanied by additional

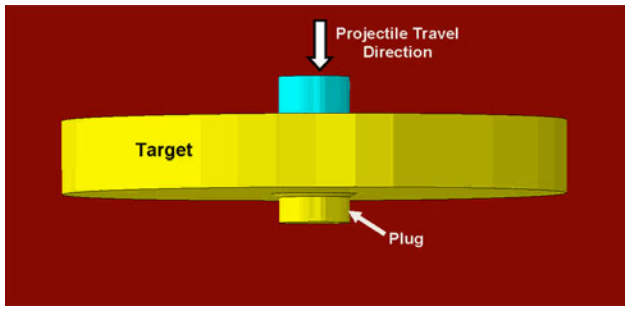

Fig. 6 Schematic representation of the plugging failure mechanism

failure modes (primarily front face/back face petaling and back face spalling), and the extent of these additional failure mechanisms is mainly controlled by the target material hardness and fracture toughness.

Plugging failure is generally assumed to be the result of shear cracking promoted by the formation of adiabatic plastic-shear bands within the target plate material surrounding the advancing (typically blunt) projectile (Ref 21, 23, 26). Owing to the pronounced localization of deformation, plastic deformation, damage, and fracture within the plastic-shear bands are the dominant modes of energy absorption in the present case, although, in the case of plug formation and ejection, some kinetic energy is transferred to the expelled plug.

In the case of plugging-dominated failure, the functional relationship between the ballistic limit and the material hardness, Fig. 5(b), is found to be qualitatively similar to that observed in the case of ductile hole enlargement-dominated failure, Fig. 5(a). The loss of ballistic limit at the highest hardness levels is again related to the accompanied reduction in the material fracture toughness and the occurrence of back face spalling. Generally, the critical hardness level at which spalling-induced loss of ballistic limit begins is lower in the case of the plugging-dominated failure. This finding is generally linked to the higher levels of the shear strain attained in the case of plugging failure promoting blunt-projectile impact. Furthermore, it should be noted that the loss of the ballistic limit under plugging-dominated failure in the highly over-aged HAZ/TMAZ material is not as severe (often, only half of that observed in the case of ductile hole enlargement failure) (Ref 1). A potential explanation for this behavior will be provided below.

2.4 Spalling

This type of failure mechanism involves the detachment of target material at rear face due to the presence of sufficiently high through-the-thickness tensile stresses. A schematic of this failure mechanism, when operating within the HAZ/TMAZ regions of the weld, is depicted in Fig. 7(a). Spalling failure is typically associated with a loss of the material through-the-thickness toughness and usually gives rise to a substantial increase in the size of the projectile exit hole (in the case of target defeat). As mentioned above, this mode of failure is dominated by the normal through-the-thickness stresses. Such stresses can arise from a number of sources such as reflection of the incident shock wave from the target back face.

As seen in Fig. 7(a), spalling in the HAZ/TMAZ weld regions appears to be associated with cracking parallel to the rolling plane, suggesting a relationship between the material's

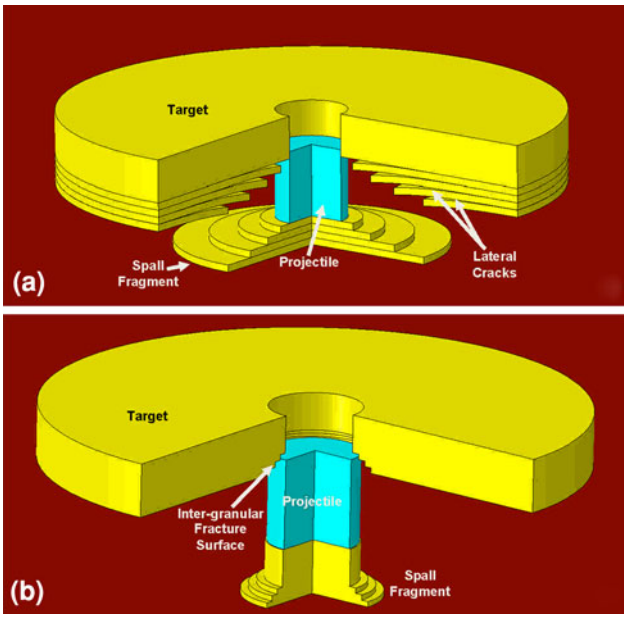

Fig. 7 Schematic representation of the spalling failure mechanism within the: (a) HAZ/TMAZ regions; and (b) the weld nugget region

as-rolled texture (associated with a microstructure in which most of the high angle grain boundaries are co-planar with the rolling plane) and its through-the-thickness mechanical properties. Specifically, the material acquires a low resistance toward grain boundary de-cohesion parallel to the target surfaces. In sharp contrast, in the case of the weld nugget, back face failure involves the formation of conical cracks emanating from the projectile head, Fig. 7(b). This finding is related to the fact that, in this weld region, due to dynamic recrystallization, grain structure is very fine and fairly equiaxed, while the orientation of the grain boundaries is quite random. Hence, no preferential spall crack extension parallel to the target faces takes place in this case.

As discussed above, the loss of ballistic performance at high hardness levels within the FSW joint is related to the onset of spalling. However, spall nucleation mechanism may differ in the case of ductile hole enlargement and plugging failure-dominated regimes. In the case of the ductile hole enlargement failure regime, strain localization is not generally considered as an important factor, and spall formation is controlled by grain boundary de-cohesion. Consequently, over-aging which causes extensive grain-boundary precipitation and the associated loss in the grain boundary cohesive strength lead to the aforementioned ca. 20% reduction in V_{50}. In the case of plugging failure-dominated regime, on the other hand, plastic-shear localization plays a major role in the onset of spalling. In other words, adiabatic shear bands which traverse several grains tend to cause cracking along the grain boundaries they cross. The growth and coalescence of these cracks leads to spall formation. Thus, when analyzing spalling within the over-aged FSW-joint material, one must recognize that while intergranular precipitation compromises grain-boundary cohesion strength, intragranular precipitation provides additional resistance to plastic-shear localization. Hence, in this case, the positive effect of delaying the onset of adiabatic plastic-shear band formation can outweigh the negative effect associated with the loss of grain boundary cohesion strength. It is then not surprising that, as mentioned above, the over-aging-induced loss of ballistic performance in the case of plugging-dominated failure regime is generally less severe than that observed in the case of ductile hole enlargement-dominated failure.

The analysis of the spall failure mode presented above brings out an additional observation. That is, the ballistic limit is not generally controlled by a single material property (e.g., hardness), but rather, various aspects of the material microstructure can affect the ballistic performance of a weldment.

3. Modeling of FSW Joint Failure Mechanisms

In the previous section, a brief overview was given of the basic physics of the four FSW joint failure mechanisms and of the role they play in controlling the ballistic limit of the armor. In this section, an attempt is made to collect the available and to derive the lacking relations quantifying the contribution of these failure modes to the target ballistic limit.

3.1 Front/Impacted and Back/Rear Face Petaling

As mentioned earlier, this mode of failure makes a small overall contribution to the ballistic limit of thick armor plates. Consequently, no attempt was made here to model and/or assess the role of this failure mechanism in the overall ballistic performance of FSWed thick aluminum-armor structures.

3.2 Ductile Hole Enlargement

The ductile hole enlargement failure mechanism is the most often modeled using the so-called "cavity expansion theory (CET)" (Ref 23, 24, 27-29). Within CET, target penetration by a (rigid, ogive-nose) projectile is treated as a problem of radial expansion of the associated (cylindrically shaped) cavity within the target. By combining the governing mass and the momentum conservation equations with the elastic-plastic material constitutive relations for the target, a functional relation is first established between the axial force opposing target penetration and the cavity-expanding radial stress (σ_s). The latter quantity, σ_s, is next correlated with the target-material stiffness and strength (including strain-hardening) parameters and with the cavity expansion rate. By employing the Newton's second law, and by ignoring the contribution of the radial expansion inertia to σ_s, the ballistic limit V_{50} is computed as the projectile minimal incident velocity required for the projectile to traverse the entire target thickness. The resulting ballistic-limit relation can be represented as (Ref 30)

$$V_{50} = \left(\frac{2\pi a^2 h \sigma_s}{m}\right)^{1/2} \quad \text{(Eq 1)}$$

where a is the projectile shank radius, m is the projectile mass, and h the target thickness.

For a nonlinear strain-hardening target material with the post-yield uniaxial stress σ_u vs. uniaxial strain ε_u , relation is being defined as

$$\sigma_u = Y\left(\frac{E\varepsilon_u}{Y}\right)^n \quad \text{(Eq 2)}$$

where Y is the quasi-static yield strength, E is Young's modulus, and n is the strain hardening exponent; σ_s can be expressed as

$$\sigma_s = \frac{Y}{\sqrt{3}}\left(1 + \left[\frac{E}{\sqrt{3}Y}\right]^n \int_0^b \frac{(-\ln x)^n}{(1-x)}\,dx\right), \quad b = 1 - \frac{\sqrt{3}Y}{E} \tag{Eq 3}$$

It should be noted that Eq 3 defines the quasi-static stress required to create and grow a cylindrical cavity from zero initial radius within an incompressible target material, the constitutive behavior of which is defined by Eq 2. Furthermore, it should be noted that while the integrand in Eq 3 has a singularity at $x = 0$, the singularity is of an integrable character. Thus, the integral in this equation can be readily evaluated.

By combining Eq 1 and 3, one obtains

$$V_{50} = \left(\frac{2\pi a^2 h\left(\frac{Y}{\sqrt{3}}\left(1 + \left[\frac{E}{\sqrt{3}Y}\right]^n \int_0^b \frac{(-\ln x)^n}{(1-x)}\,dx\right)\right)}{m}\right)^{\frac{1}{2}},$$

$$b = 1 - \frac{\sqrt{3}Y}{E} \tag{Eq 4}$$

Examination of Eq 4 reveals a nonlinear relationship between material strength (hardness) and the ballistic limit (V_{50}). While this finding appears to be in conflict with the corresponding experimentally observed linear relationship between the same two quantities, the results displayed in Fig. 5(a) suggests that the extent of nonlinearity in the V_{50} vs. σ_u relation, as predicted by Eq 4 is relatively small. It should be noted that the curve displayed in Fig. 5(a) was obtained using stereotypical aluminum-alloy material parameters: $E = 70$ GPa, $Y = 250$ MPa and $n = 0.15$.

It is interesting to note that, when Eq 4 is used to predict target ballistic limit (a high strain-rate phenomenon), good theory/experiment agreement is generally attained although quasi-static material properties are used. At high deformation rates (and in the presence of the accompanying thermal effects), material (dynamic) properties are expected, in general, to be different form their quasi-static room-temperature counterparts. The high level of experiment/theory agreement achieved is often explained using the fact that, under ballistic loading, material deformation is nearly adiabatic (i.e., heat conduction is practically absent), and hence, ductile hole enlargement is controlled by the plastic deformation of the surrounding material at ambient temperature (at which aluminum alloys typically show very little strain-rate sensitivity).

3.3 Plugging

Plugging failure is generally assumed to be the result of shear cracking promoted by the formation of adiabatic plastic-shear bands within the target plate material surrounding the advancing blunt projectile (Ref 21, 23, 26). Plugging failure is generally modeled by combining the conservation equations and material constitutive relations with one of the adiabatic plastic-shear instability theories (e.g., Ref 26).

The phenomenon of adiabatic plastic-shear instability and its subsequent localization has been the subject of intense research over the last 30 years. It is generally accepted that the essential physics behind adiabatic plastic-shear instability/localization is well understood, although reliable quantitative relations between the onset of this failure mechanism and the material properties and loading conditions are still lacking. Plastic shear strain instability occurs at a given material point when, in the course of loading, strain-induced hardening becomes over-matched by the strain-induced softening processes. Under such conditions, the local rate of change of the maximum shear stress, τ, with the associated shear strain, γ, becomes non-positive, i.e.,

$$\frac{d\tau}{d\gamma} = \left.\frac{\partial\tau}{\partial\gamma}\right|_{T,\dot{\gamma}} + \left.\frac{\partial\tau}{\partial\dot{\gamma}}\right|_{T,\gamma}\frac{d\dot{\gamma}}{d\gamma} + \left.\frac{\partial\tau}{\partial T}\right|_{\dot{\gamma},\gamma}\frac{dT}{d\gamma} <= 0 \tag{Eq 5}$$

where a raised dot is used to denote a time derivative, and T denotes temperature. It should be noted that Eq 5 is obtained by applying the chain rule to differentiation of τ with respect to γ. This equation simply recognizes the fact that a change in γ affects τ both directly and indirectly (through the associated changes in the shear strain rate, $\dot{\gamma}$, and temperature.

In Eq 5, under the adiabatic condition, $(dT/d\gamma)$ can be set equal to τ/C, where C is the volumetric specific heat. As far as the remaining derivatives on the right-hand side of Eq 5 are concerned, their functional relationship depends on the $\tau(\gamma, \dot{\gamma}, T)$ relation used. For example, if strain hardening and strain-rate sensitivity relations are both assumed to be of a parabolic character with the corresponding exponents denoted respectively as n and m, Eq 5 can be re-written as

$$\gamma_c = \frac{n}{\left(\frac{-1}{C}\left.\frac{\partial\tau}{\partial T}\right|_{\gamma,\dot{\gamma}} - \frac{m}{\dot{\gamma}}\frac{d\dot{\gamma}}{d\gamma}\right)} \tag{Eq 6}$$

where γ_c is a (minimum) critical value of the shear strain at the onset of plastic shear-strain instability at which $(d\tau/d\gamma) = 0$. Equation 6 can be further simplified in the high strain-rate regime ($\dot{\gamma} > 100\ s^{-1}$) and for a typical range of values of the strain-rate sensitivity exponent ($0 < m < 1.0$) as

$$\gamma_c = -\frac{Cn}{\left(\left.\frac{\partial\tau}{\partial T}\right|_{\gamma,\dot{\gamma}}\right)} \tag{Eq 7}$$

Examination of Eq 7 reveals that the onset of plastic-shear strain instability and localization is delayed in materials in which

(a) volumetric specific heat is relatively large and, hence, the associated adiabatic temperature increase is relatively small;
(b) strain hardening effects are strong and can effectively counteract the effect of various softening processes; and
(c) temperature sensitivity of the material strength is not pronounced, so that local heating does not significantly reduce the material resistance toward plastic deformation.

It should be noted that Eq 6 and 7 provide functional relationships between the critical shear strain at the onset of plastic shear strain localization and the material constitutive response (properties) but do not explicitly deal with the target-material ballistic limit. While the phenomenon of shear strain localization dominates the plugging mode of failure, it is a formidable task to establish functional relationships between the associated ballistic limit and the material's propensity to plastic shear-instability (as quantified by the critical shear strain, γ_c). Simply stated, the plugging failure-controlled ballistic limit is expected to increase with an increase in material hardness (as supported by the results displayed in Fig. 5b), although this effect is not accounted for in Eq 6 and 7. Thus, one would expect that high-hardness and high strain-hardening target materials would, in general, possess superior

ballistic performance. However, in the case of FSW joints, there is a trade-off between material hardness and its strain-hardening potential (i.e., these two material properties cannot be changed independently). In other words, in weld zones further away from the center line, hardness levels are expected to be high while the strain-hardening potential is expected to be low. Converse is true for the weld zones located near the center line. These findings provide an explanation for the results displayed in Fig. 5(b). That is, at the lowest hardness levels, the onset of plastic shear-strain instability is greatly delayed. However, the overall target material hardness and, hence, projectile kinetic-energy absorption remain low. In other words, the energy absorbed by the target can be defined as an integral of stress over the associated strain path until localization. In this case, while the upper limit of this integral (γ_c) is large, the stress values remain small resulting in a small value of the integral. As the target material hardness increases, its ballistic limit increases due to the accompanying higher ability for energy absorption. In other words, the effect of an increase in the material strength more than compensates for the accompanying reduction in γ_c. At the highest hardness levels, the target material's ability to absorb projectile energy decreases because material becomes highly prone to plastic strain localization. In other words, while the material resistance to plastic deformation is high, mat material's high propensity toward plastic shear-strain localization leads to an early failure.

The analysis presented above shows a complicated interplay between material hardness/strength, its strain-hardening behavior, and its plugging failure-controlled ballistic limit. It is, hence, not surprising that there is no broadly accepted functional relationship between the plugging failure-controlled ballistic limit and the target material constitutive response/properties. To overcome this lack of the appropriate functional relationship for the plugging failure-controlled ballistic limit, a simple phenomenological model is developed below. The model presented assumes that the projectile (of a right-circular cylindrical shape) remains undeformed during impact. Then, the model postulates that the kinetic energy of the projectile at the onset of plugging is exactly balanced by the work of plastic deformation in the shear-localization region surrounding the projectile as

$$\frac{1}{2}\rho_{\mathrm{Proj}}\pi R_{\mathrm{Proj}}^2 h_{\mathrm{Proj}} V_{50}^2 = 2\pi R_{\mathrm{Proj}} h_{\mathrm{Target}} \delta R_{\mathrm{Shear}} \int_0^{\gamma_c} \tau \mathrm{d}\gamma \qquad \text{(Eq 8)}$$

where ρ denotes density, R the radius, h the thickness/height, δR the radial thickness. and subscripts "Proj," "Target," and "Shear" represent the appropriate quantities in the projectile, target, and the plastic shear localization zones. It should be noted that the present model contains only one adjustable parameter: $\delta R_{\mathrm{Shear}}$.

Application of Eq 8 to the establishment of a functional relationship between the target material ballistic limit and its hardness in the case of the plugging-dominated failure for the aluminum-alloy grade used in Ref 1 is depicted in Fig. 5(b). The value of $\delta R_{\mathrm{Shear}}$ is adjusted in this case for an optimal fit of the experimental results also shown in the same figure. It is seen that the experiment/computation agreement is reasonable.

3.4 Spalling

As mentioned above, spalling failure typically occurs at the target back face, is associated with a loss of the material through-the-thickness toughness and usually gives rise to a substantial increase in the size of the projectile exit hole (in the case of target defeat). As seen in Fig. 5(a), this also gives rise to a loss in the target-material ballistic limit in the FSW (HAZ and TMAZ) zones associated with the highest levels of material hardness (i.e., the lowest levels of the material through-the-thickness toughness). The results displayed in Fig. 5(a) should be interpreted in the following way: (a) at the lowest hardness levels and, hence, the highest through-the-thickness toughness levels of the (HAZ/TMAZ zone) target material, the target is defeated in a ductile fashion and involves back face petaling; (b) as the target material hardness increases and the associated through-the-thickness toughness decreases, spall resistance decreases but remains higher than that for ductile failure; and (c) at the highest target material hardness levels (found in the base metal and the adjacent HAZ), the spall resistance falls below that for the ductile failure (due to a loss in the through-the-thickness toughness) and back face spalling takes place compromising the target ballistic limit.

As indicated in Fig. 7(a), spall failure within the HAZ/TMAZ zones is associated with the formation of lateral cracks which propagate along the grain boundaries parallel to the target faces. Furthermore, as suggested by Fig. 5(a), HAZ/TMAZ spall fracture gives rise to a loss in the ballistic limit. On the other hand, as suggested by Fig. 7(b), spall failure within the weld nugget, while still being inter-granular in character, behaves more as a ductile failure mode (and, hence, is often not associated with a significant reduction in the ballistic performance).

Spall failure has been investigated extensively over the last thirty years, yet many aspects of this important phenomenon are still unresolved (e.g., Ref 31). It is, hence, no surprise that there is no broadly accepted functional relation for the spall failure-dominated ballistic limit. No attempt will be made in this study to derive this functional relationship for the following reasons:

(a) In the case of the HAZ/TMAZ zones, spall fracture shows an affect only at the highest level of material hardness (i.e., in the base metal and in the adjacent HAZ region), while the associated loss of ballistic limit is relatively small;
(b) Spall failure affects even less the ballistic limit of the weld nugget; and
(c) The subject matter is quite complex and will be given adequate attention in our future study.

4. Spatial Distribution of the Ballistic Limit Within the FSW Joint

In this section, an attempt is made to predict spatial distribution of the ballistic limit within a prototypical FSW butt joint. Toward this end, the thermomechanical finite-element-based computational analysis of the FSW process developed in a series of our prior articles (Ref 32-40) has been combined with the ballistic-impact-induced failure models (overviewed in the previous section). Since a detailed account of our FSW process-modeling approach can be found in our prior study (Ref 32-40), only a brief overview of the same is given in the next section. This is followed by a section in which the results pertaining to the spatial distribution of ballistic limit within a prototypical FSW butt joint are presented and discussed.

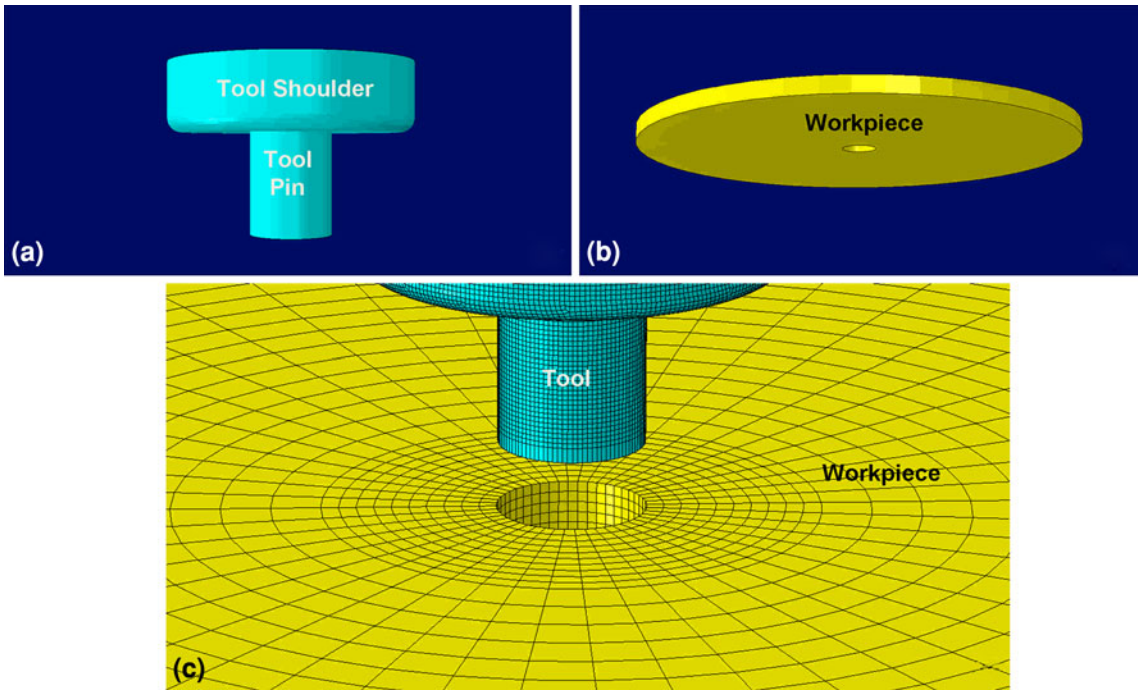

Fig. 8 Geometrical models of the: (a) FSW tool; (b) the workpiece; and (c) a close-up view of the corresponding FSW-meshed models

4.1 FSW Process Modeling

The FSW process model developed in our prior study (Ref 32-40) is based on a fully coupled thermomechanical finite-element analysis and involves the use of the workpiece-material models which account for the evolution of material microstructure and properties during the joining process. The essential components of this model can be summarized in the following sections.

4.1.1 Computational Domain and Meshed Models. The computational domain used typically consists of a circular plate/workpiece (with a concentric through-the-thickness circular hole) and a two-part tool (consisting of a solid right circular cylindrical pin, at the bottom, and a larger-radius circular-disk-shaped shoulder, on the top), Fig. 8(a) and (b).

The workpiece and the FSW tool geometrical models described above are typically meshed using 15000-20000 first-order eight-node reduced-integration hexahedral thermomechanically coupled solid elements. A close-up view of the typically meshed models is depicted in Fig. 8(c).

4.1.2 Computational Algorithm. The FSW process is analyzed computationally using a fully (two-way) coupled thermomechanical finite-element algorithm within which heat dissipation associated with plastic deformation and tool/work-piece interfacial friction-sliding is treated as a source in the governing heat conduction equation(s), while the effect of temperature on the mechanical response of the work-piece material is taken into account through the use of a temperature-dependent work-piece material model. Since the material within the FSW joint is subjected to large strains and motion, purely Lagrangian formulation which is prone to excessive mesh distortions is inadequate and, instead, an arbitrary Lagrangian Eulerian (ALE) formulation is used. The fully coupled thermomechanical process model for FSW is implemented in and solved using ABAQUS/Explicit (Ref 41), a general purpose explicit finite element solver. It should be noted that, at the beginning of a typical finite-element simulation of the FSW process, tool plunging (without tool travel), is first analyzed. Once convergence is obtained, the tool travel stage is analyzed and the simulation terminated at a point when the solution reaches a steady state. The results reported later in this section pertain to this steady-state condition.

4.1.3 Sources of Heat. As mentioned earlier, both plastic deformation and frictional sliding are treated as heat sources. To account for the fact that a small fraction of the plastic-deformation work is stored in the form of crystal defects, 95% of which was (arbitrarily) assumed to be dissipated in the form of heat. As far as heat generation due to frictional sliding is concerned, it is assumed that its rate scales with the product of contact tangential traction and the sliding rate, and that 100% of this energy is dissipated in the form of heat.

4.1.4 Initial and Boundary Conditions. The analysis is carried out by prescribing from the onset a constant rotational velocity and a constant downward pressure to the tool. Instead of assigning a travel velocity to the tool along the (postulated) butting surfaces of the work-piece, the work-piece material is forced to move through the work-piece computational domain at the tool-travel velocity but in the opposite direction. This was accomplished by prescribing from the onset of the FSW simulation a constant in-flow workpiece material velocity in a direction opposite to that of tool travel.

Additional boundary conditions employed are as follows:

(a) zero normal-velocity conditions applied over the bottom face of the workpiece to mimic the restraining effect of the work-piece rigid backing plate;
(b) the standard convective boundary conditions are applied over free surfaces of the work-piece and the tool; and
(c) enhanced convection boundary conditions are applied over the bottom face of the work-piece (to mimic the effect of enhanced heat extraction through the work-piece backing plate).

It should be noted that, due to the nature of the initial and boundary conditions used, the circular plate displayed in Fig. 8(b) represents not the entire work-piece but rather a circular (instantaneous) region around the tool in the otherwise infinitely long workpiece.

4.1.5 Contact Interactions. To enable the transfer of normal and tangential tractions between the workpiece and the tool, the appropriate contact algorithms are used. Specifically, transfer of normal tractions is modeled using the so-called "*penalty algorithm*" within which the normal traction magnitude scales with the extent of workpiece/tool contact-surface penetration. As far as the tangential tractions are concerned, they are transferred via a modified coulomb friction-based "slip/stick" algorithm within which the tangential traction magnitude is defined as a product of the static/kinetic friction coefficient and the tangential traction magnitude. As mentioned earlier, heat generated due to frictional sliding scales with the product of contact tangential traction and the sliding rate. This heat is partitioned between the workpiece and the tool using a functional relationship based on the thermal properties of the tool and workpiece materials (Ref 32). It should be noted that, although, in some of the present FSW simulations, the tool was modeled as a rigid body, meshing of the tool had to be undertaken to define the contact surfaces which are used in the work-piece/tool contact-interaction definitions.

4.1.6 Material Models. Since the tool normally experiences relatively little deformation during FSW, the tool material is modeled using either a rigid or a linear thermoelastic formulation and temperature-dependent material's thermomechanical properties.

The work-piece material is assumed to be isotropic, linear-elastic and strain-hardenable, strain-rate sensitive, thermally softenable plastic material, and is modeled using the modified Johnson-Cook material model (Ref 32). The key modifications in this model relative to its conventional formulation deal with the inclusion of various microstructure-evolution equations which enable the prediction of the changes in the material local microstructure and properties during FSW.

4.2 Spatial Distribution of V_{50} Within the FSW Butt Joint

Before presenting and discussing the results concerning the spatial distribution of V_{50} within the weld, an example of the associated results (obtained using the aforementioned fully coupled thermomechanical finite-element analysis of the FSW process) pertaining to the spatial distribution of the material grain size and yield strength are displayed in Fig. 9(a) and (b), respectively. These results pertain to the case of AA5083-H131 (a non-age-hardenable, solid-solution-strengthened, strain-hardened/stabilized Al-Mg-Mn alloy), a workpiece thickness of 25.4 mm, tool rotational speed of 250 rpm, and tool translational speed of 1.9 mm/s.

The results displayed in Fig. 9(a) pertain to the average grain size distribution over a transverse cut of the weld for the case of AA5083-H131 with an initial grain size of 50 μm. It is seen that there is a region with a slightly increased grain-size and another region with a considerably reduced grain-size. The two regions can be assumed to comprise of HAZ/TMAZ and weld nugget/flow-arm zones, respectively. These grain-size distribution predictions are generally in a good agreement with their experimental counterparts obtained using the conventional metallographic examinations and reported in Ref 39.

The results displayed in Fig. 9(b) pertain to the yield-strength distribution over a transverse cut of the weld for the case of AA5083-H131 with initial yield strength of 167 MPa. The results displayed in this figure suggest the presence of three weld regions (not counting the base-metal): (a) the inner-most region which comprises the weld nugget and flow-arm zones. The intermediate yield strength levels found in this region appear to be the result of the competition between grain-size refinement-induced hardening and the dynamic recrystallization-induced softening; (b) The intermediate high-strength region (which corresponds to the TMAZ zone) in which the strain hardening effects play a dominant role in controlling material strength; and (c) The (HAZ) region adjacent to the base-metal in which, due to the absence of plastic deformation and exposure to slightly elevated temperatures, very small reductions in the material strength relative to the base metal strength level (167 MPa) are observed.

As discussed in Sect. 3, depending on the geometry of the projectile, either hole-enlargement failure or plugging failure may control the ballistic limit of the target. Consequently, separate predictions regarding the spatial distribution of V_{50} within an FSW butt joint are made for these two modes of target penetration.

4.2.1 Ductile Hole-Enlargement Failure Mode. In this case, Eq 4 (along with the local values for the material Young's Modulus, material yield strength and strain-hardening exponent) is used to compute the corresponding values of V_{50} velocity. Only the case of a 7.62 mm caliber, 8.2 g, ogival-nose, steel jacketed, hard tungsten core (1400 Hv), AP projectile is considered. The Young's Modulus of the target is treated as a microstructure-insensitive property and assigned a constant value throughout the weld. The spatial distribution of the target-material yield strength within the joint is taken from Fig. 9(b). As far as the strain hardening exponent is concerned, its spatial distribution within the weld was assessed using the

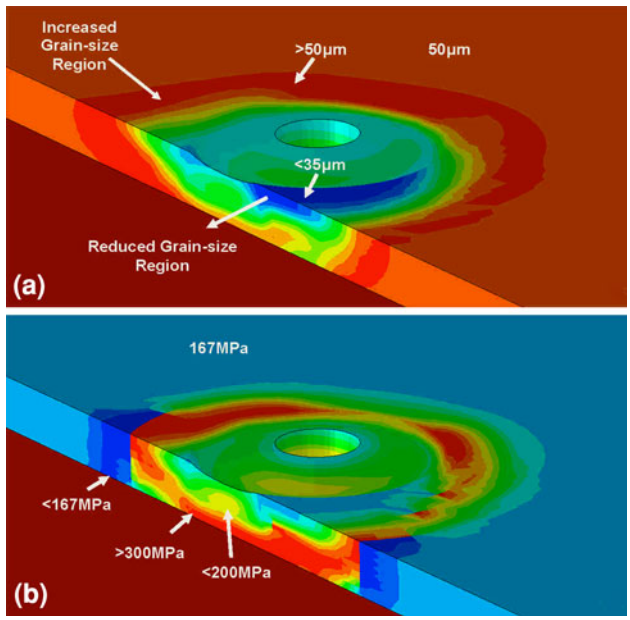

Fig. 9 Typical spatial distributions of: (a) the grain-size; and (b) the yield strength across a transverse section of a FSW-joint in AA5083-H131 with an initial grain size of 50 μm and initial yield strength of 167 MPa

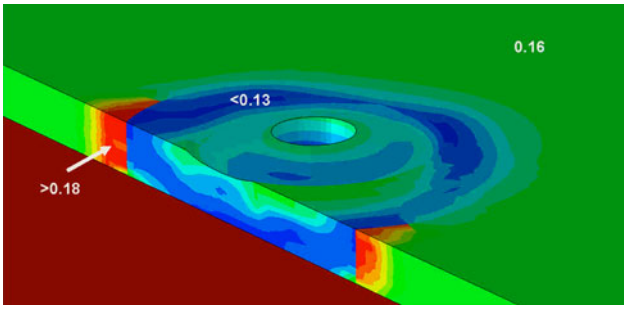

Fig. 10 Typical spatial distributions of the strain hardening exponent across a transverse section of a FSW-joint in AA5083-H131 with an initial strain hardening exponent, $n = 0.16$

results of our on-going micro-tensile test experiments (Ref 42), Fig. 10. A comparison of the results displayed in Fig. 9(b) and 10 shows that, as expected, as the material yield strength within the weld increases, the strain hardening potential, as quantified by the exponent n, of the same material decreases.

The procedure described above yielded the spatial distribution of V_{50} within the FSW butt weld as shown in Fig. 11(a). Examination of this figure reveals that (a) there are regions within the FSW joint within which the ballistic limit has been reduced (by ca. 10%) below the level observed in the base metal ca. 597 m/s; (b) the low V_{50} region within the weld coincides with the low strength region within the same weld. This finding is fully consistent with the CET predictions given in Fig. 5(a); and (c) in the particular case investigated here the low V_{50} region within the FSW joint represents a relatively small volume fraction ($<10\%$) of the total weld volume. Hence, the presence of this zone may not greatly compromise the overall ballistic performance of the FSWed armor structure.

4.2.2 Plugging Failure Mode. In this case, Eq 7 and 8 (along with the values for the volumetric heat capacity, material yield strength, strain-hardening exponent, and the temperature sensitivity of the material strength $\frac{\partial \tau}{\partial T}\big|_{\gamma,\dot{\gamma}}$) are used to compute the corresponding values of V_{50} velocity. Only the case of a 20-mm caliber, 53 g, blunt, chamfered right-circular cylindrical steel FSP is considered. The volumetric heat capacity of the target is treated as a microstructure-insensitive property and assigned a constant value throughout the weld. The spatial distribution of the target-material yield strength within the joint is again taken from Fig. 9(b), and the strain hardening exponent is taken from Fig. 10. As far as the temperature sensitivity of the material strength is concerned, it is assumed to scale with the material strength. In other words, as the material strength increases because of the effects of strain hardening and grain size refinement, the material microstructure becomes less stable and more prone to changes which give rise to softening.

The procedure described above yielded the spatial distribution of V_{50} within the FSW butt weld as shown in Fig. 11(b). Examination of the results displayed in this figure and their comparison with the results displayed in Fig. 11(a), shows that the overall spatial distribution of the ballistic limits with respect to the plastic shear localization and ductile hole enlargement failure mechanisms are fairly similar. Also, the V_{50} values pertaining to the plastic-shear localization failure mode are consistently lower than their ductile hole enlargement failure counterparts which is fully consistent with the results displayed in Fig. 5(a) and (b).

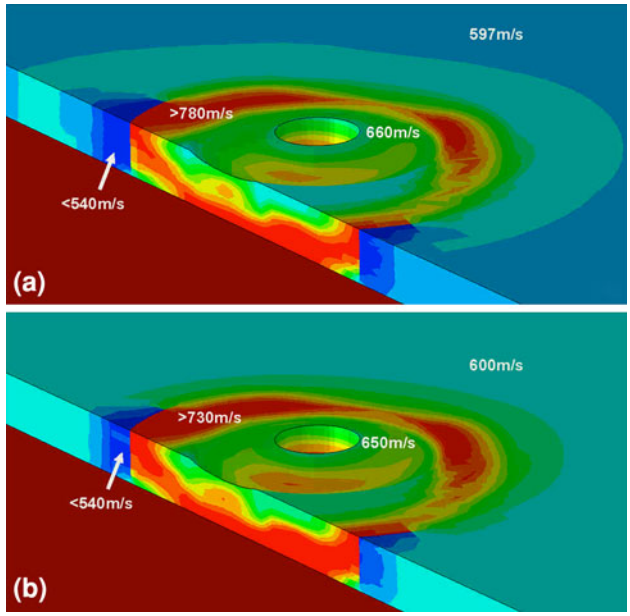

Fig. 11 Typical spatial distributions of the V_{50} for the case of: (a) ductile hole enlargement failure; and (b) plugging failure-controlled target penetration

5. Summary and Conclusions

Based on the results presented and discussed in the present study, the following main summary remarks and conclusions can be made:

1. A new procedure is proposed for predicting spatial distribution of the ballistic limit within a prototypical FSW butt joint.
2. This procedure combines the results of the FSW process modeling, basic physical-metallurgy principles concerning microstructure/property relations and the fracture mechanics concepts related to the key blast/ballistic-impact failure modes (i.e., front/back-face petaling, ductile hole enlargement, plugging and spallation).
3. The procedure is applied to the case of solid-solution strengthened and cold-worked aluminum alloy armor FSWed test structure.
4. For the specific cases of the armor-piercing and fragment-simulating projectile ballistic impacts, the procedure clearly revealed the loss in the ballistic limit within the weld. However, the extent of that loss was not very significant suggesting that the overall ballistic performance of the FSW armor test structure was not seriously compromised.

Acknowledgments

The material presented in this article is based on the study supported by two Army Research Office sponsored grants (W911NF-11-1-0207 and W911NF-09-1-0513) and two U.S. Army/Clemson University Cooperative Agreements (W911NF-04-2-0024 and W911NF-06-2-0042).

References

1. A. Sullivan, C. Derry, J.D. Robson, I. Horsfall, and P.B. Prangnell, Microstructure Simulation and Ballistic Behavior of Weld Zones in Friction Stir Welds in High Strength Aluminium 7xxx Plate, *Mater. Sci. Eng. A*, 2011, **528**, p 3409–3422
2. W.M. Thomas, E.D. Nicholas, J.C. Needham, M.G. Murch, P. Temple-Smith, and C.J. Dawes, "Friction Stir Butt Welding," International Patent Application No. PCT/GB92/02203, 1991
3. M. Grujicic, B. Pandurangan, K.L. Koudela, and B.A. Cheeseman, A Computational Analysis of the Ballistic Performance of Light-Weight Hybrid-Composite Armors, *Appl. Surf. Sci.*, 2006, **253**, p 730–745
4. H. Liu, H. Fulii, M. Maeda, and K. Nogi, Tensile Properties and Fracture Locations of Friction-Stir Welded Joints of 6061-T6 Aluminium Alloy, *J. Mater. Sci. Lett.*, 2003, **22**, p 1061–1063
5. W.B. Lee, C.Y. Lee, W.S. Chang, Y.M. Yeon, and S.B. Jung, Microstructural Investigation of Friction Stir Welded Pure Titanium, *Mater. Lett.*, 2005, **59**, p 3315–3318
6. W.M. Thomas and E.D. Nicholas, Friction Stir Welding for the Transportation Industries, *Mater. Des.*, 1997, **18**, p 269–273
7. J.Q. Su, T.W. Nelson, R. Mishra, and M. Mahoney, Microstructural Investigation of Friction Stir Welded 7050-T651 Aluminum, *Acta Mater.*, 2003, **51**, p 713–729
8. O. Frigaard, Ø. Grong, and O.T. Midling, A Process Model for Friction Stir Welding of Age Hardening Aluminum Alloys, *Metall. Mater. Trans. A*, 2001, **32**, p 1189–1200
9. M.W. Mahoney, C.G. Rhodes, J.G. Flintoff, R.A. Spurling, and W.H. Bingel, Properties of Friction-Stir-Welded 7075 T651 Aluminum, *Metall. Mater. Trans. A*, 1998, **29**, p 1955–1964
10. C.G. Rhodes, M.W. Mahoney, W.H. Bingel, R.A. Spurling, and C.C. Bampton, Effect of Friction Stir Welding on Microstructure of 7075 Aluminum, *Scr. Mater.*, 1997, **36**, p 69–75
11. G. Liu, L.E. Murr, C.S. Niou, J.C. McClure, and F.R. Vega, Microstructural Aspects of the Friction-Stir-Welding of 6061-T6 Aluminum, *Scr. Mater.*, 1997, **37**, p 355–361
12. M. Grujicic and G. Arakere, Computational Investigation of Hardness Evolution During Friction-Stir Welding of AA5083 and AA2139 Aluminum Alloys, *J. Mater. Eng. Perform.*, 2011, **20**(7), p 1097–1108
13. J.C. Bassett and S.S. Birley, *Proceedings of the 2nd Symposium on Friction Stir Welding*, TWI, 2000 (on CD)
14. K. Sampath, *Adv. Mater. Process.*, 2005, **163**, p 27–29
15. C. Garcia-Cordovilla, E. Louis, and A. Pamies, Microstructure and Susceptibility to Stress Corrosion Cracking of Al-Zn-Mg Weldments (AA-7017), *Mater. Sci. Eng.*, 1994, **174A**, p 173–186
16. C. Johnson, Amphibian Warfare, Nov–Dec, 1998, p 2–16
17. K.J. Colligan, P.J. Konkol, J.J. Fisher, and J.R. Pickens, Friction Stir Welding Demonstrated for Combat Vehicle Construction, *Weld. J.*, 2003, **82**(3), p 34–40
18. K.J. Colligan, J.J. Fisher, J.E. Cover, and J.R. Pickens, *Adv. Mater. Process.*, 2002, **160**(9), p 39–41
19. P.L. Threadgill, A.J. Leonard, H.R. Shercliff, and J.P. Withers, Friction Stir Welding of Aluminum Alloys, *Int. Mater. Rev.*, 2009, **54**(2), p 49–93
20. M.M.Z. Ahmed, B.P. Wynne, W.M. Rainforth, and P.L. Threadgill, *Proceedings of the 7th Symposium on Friction Stir Welding*, TWI, Awaji Island, 2008 (on CD)
21. G.G. Corbett, S.R. Reid, and W. Johnson, Impact Loading of Plates and Shells by Free-Flying Projectiles: A Review, *Int. J. Impact Eng.*, 1996, **18**(2), p 141–230
22. K.S. Kumar, D. Singh, and T. Bhat, Studies on Aluminum Armour Plates Impacted by Deformable and Non-Deformable Projectiles, *Mater. Sci. Forum.*, 2004, **465–466**, p 79–84
23. T. Børvik, O.S. Hopperstad, and K.O. Pedersen, Fracture Mechanisms of Aluminum Alloy AA7075-T651 Under Various Loading Conditions, *Int. J. Impact Eng.*, 2010, **37**, p 537–551
24. T. Børvik, M.J. Forrestal, O.S. Hopperstad, T.L. Warren, and M. Langseth, Perforation of AA5083-H116 Aluminium Plates with Conical-Nose Steel Projectiles—Calculations, *Int. J. Impact Eng.*, 2009, **36**, p 426–437
25. M.R. Edwards and A. Mathewson, The Ballistic Properties of Tool Steel as a Potential Improvised Armor Plate, *Int. J. Impact Eng.*, 1997, **19**, p 297–309
26. T. Børvik, J.R. Leinum, J.K. Solberg, O.S. Hopperstad, and M. Langseth, Observations on Shear Plug Formation in Weldox 460 E Steel Plates Impacted by Blunt-Nosed Projectiles, *Int. J. Impact Eng.*, 2001, **25**, p 553–572
27. M.J. Forrestal, V.K. Luk, and N.S. Brar, Penetration of Aluminum Armor Plates with Conical-Nose Projectiles, *Mechanics*, 1990, **10**, p 97–105
28. A.J. Piekutowski, M.J. Forrestal, K.L. Poormon, and T.L. Warren, Ogive-Nose Steel Rods at Normal, *Int. J. Impact Eng.*, 1996, **18**, p 877–887
29. T. Børvik, A.H. Clausen, O.S. Hopperstad, and M. Langseth, Perforation of AA5083-H116 Aluminium Plates with Conical-Nose Steel Projectiles—Experimental Study, *Int. J. Impact Eng.*, 2004, **30**, p 367–384
30. A.H. Chausen, T. Børvik, O.S. Hopperstad, and A. Benallal, Flow and Fracture Characteristics of Aluminium Alloy AA5083-H116 as Function of Strain Rate, Temperature and Triaxiality, *Mater. Sci. Eng.*, 2004, **A364**, p 260–272
31. A.P. Rybakov, Spall in Non-One-Dimensional Shock Waves, *Int. J. Impact Eng.*, 2000, **24**, p 1041–1082
32. M. Grujicic, B. Pandurangan, C.-F. Yen, and B.A. Cheeseman, Modifications in the AA5083 Johnson-Cook Material Model for Use in Friction Stir Welding Computational Analyses, *J. Mater. Eng. Perform.*, doi:10.1007/s11665-011-0118-7, 2011
33. M. Grujicic, G. Arakere, B. Pandurangan, J.M. Ochterbeck, C-.F. Yen, B.A. Cheeseman, A.P. Reynolds, and M. A. Sutton, Computational Analysis of Material Flow During Friction Stir Welding of AA5059 Aluminum Alloys, *J. Mater. Eng. Perform.*, doi:10.1007/s11665-011-0069-z, 2011
34. M. Grujicic, G. Arakere, A. Hariharan, B. Pandurangan, C-F. Yen, and B.A. Cheeseman, Two-level Weld-Material Homogenization Approach for Efficient Computational Analysis of Welded Structure Blast Survivability, *J. Mater. Eng. Perform.*, doi:10.1007/s11665-011-9876-5, 2010
35. M. Grujicic, G. Arakere, A. Hariharan, and B. Pandurangan, A Concurrent Product-Development Approach for Friction-Stir Welded Vehicle-Underbody Structures, *J. Mater. Eng. Perform.*, doi:10.1007/s11665-011-9955-7, 2010
36. M. Grujicic, G. Arakere, B. Pandurangan, and A. Hariharan, Statistical Analysis of High-Cycle Fatigue Behavior of Friction Stir Welded AA5083-H321, *J. Mater. Eng. Perform.*, 2011, **20**(6), p 855–864
37. M. Grujicic, G. Arakere, B. Pandurangan, A. Hariharan, C.-F. Yen, B.A. Cheeseman, and C. Fountzoulas, Computational Analysis and Experimental Validation of the Ti-6Al-4V Friction Stir Welding Behavior, *J. Eng. Manuf.*, 2010, **224**(8), p 1–16
38. M. Grujicic, G. Arakere, B. Pandurangan, and A. Hariharan, Development of a Robust and Cost-Effective Friction Stir Welding Process for Use in Advanced Military Vehicle Structures, *J. Mater. Eng. Perform.*, 2011, **20**(1), p 11–23
39. M. Grujicic, G. Arakere, H.V. Yalavarthy, and T. He, Modeling of AA5083 Material-Microstructure Evolution During Butt Friction-Stir Welding, *J. Mater. Eng. Perform.*, 2010, **19**(5), p 672–684
40. M. Grujicic, T. He, G. Arakere, H.V. Yalavarthy, C.-F. Yen, and B.A. Cheeseman, Fully-Coupled Thermo-Mechanical Finite-Element Investigation of Material Evolution During Friction-Stir Welding of AA5083, *J. Eng. Manuf.*, 2010, **224**(4), p 609–625
41. ABAQUS Version 6.10EF, User Documentation, Dassault Systems, 2011
42. C. F. Yen, Army Research Laboratories, Work in Progress, 2012